

CFD Modeling of Wing and Body of an AUV for Estimation of Hydrodynamic Coefficients

N. M. Nouri, K. Mostafapour[†] and S. H. Hassanpour

School of Mechanical Engineering, Iran University of Science and Technology, Tehran, Iran

[†]*Corresponding Author Email: mostafapour@iust.ac.ir*

(Received July 26, 2015; accepted January 13, 2016)

ABSTRACT

Coefficients or hydrodynamic derivatives of autonomous underwater vehicles (AUVs) play a key role in their design and maneuverability. Using a suitable method to estimate these coefficients serves as a time efficient approach to raise the achievable precision in the design and control of AUVs. This paper estimates hydrodynamic derivatives of an AUV using computational fluid dynamics (CFD) for the wings and body. CFD modeling was performed to simulate captive model tests including straight line and planar motion mechanism (PMM). In such runs, the process was implemented separately for the wing and body. Experimental tests for the same AUV in the water tunnel were carried out for CFD validation. Comparing the numerical results to the experimental data, it was shown that the modeling method is able to estimate these coefficients at reasonable accuracy. The proposed modeling method was proved to be efficient in estimating hydrodynamic derivatives and hence can reduce associated computational costs with the process of detail design of AUVs.

Keywords: Hydrodynamics derivatives; Captive model test; Numerical modeling; AUV; Water tunnel.

NOMENCLATURE

$C_{1\varepsilon}, C_{2\varepsilon}, C_{\mu}$	turbulence constants	x_G	center of gravity in x-direction
D	drag force	w, \dot{w}	heave velocity and acceleration
I_{yy}	mass moment of inertia about y-axis	+	non-dimensional distance of the first node near to the wall
k	turbulent kinetic energy	Z	force the z direction
l	model length	Z_H	hydrodynamic force the z direction
L	lift force	Z_{in}	in phase components of the recorded heave force during a PMM test
m	mass of AUV	Z_{out}	out phase components of the recorded heave force during a PMM test
M	moment about y-axis	$Z_q, Z_{\dot{q}}$	linear hydrodynamic coefficient of pitch force
M_H	hydrodynamic moment about y-axis	$Z_{q q }$	nonlinear hydrodynamic coefficient of force as functions of pitch velocity
M_{in}	in phase components of the recorded heave moment during a PMM test	$Z_w, Z_{\dot{w}}$	linear hydrodynamic coefficients of heave force
M_{out}	out phase components of the recorded heave moment during a PMM test	$Z_{w w }$	nonlinear coefficient of force as functions of heave velocity
$M_q, M_{\dot{q}}$	linear hydrodynamic coefficients of pitch moment	z_0	amplitude of oscillation
$M_{q q }$	nonlinear hydrodynamic coefficient of pitch moment	A	angle of attack
$M_w, M_{\dot{w}}$	linear hydrodynamic coefficient of heave moment	ε	viscous dissipation rate of turbulent kinetic energy
$M_{w w }$	nonlinear hydrodynamic coefficient of heave moment	θ_0	angular amplitude of oscillation
P	Reynolds-averaged pressure		
q, \dot{q}	angular pitch velocity and acceleration		
Re	Reynolds number		

t	time	μ	fluid dynamic viscosity
U	model velocity	μ_t	eddy viscosity
\dot{u}	acceleration the x direction	ρ	flow density
U_i, U_j	mean velocity components of fluid	$\sigma_k, \sigma_\varepsilon$	turbulence Prandtl number for k and ε
u_i, u_j	fluctuation velocity components of fluid	ω	circular frequency of oscillation
X	force in the x direction		

1. INTRODUCTION

Due to their applications in deep-sea explorations, hydrographic surveying, and defense operations, AUVs have gained particular considerations in terms of research and development in recent years. Control and stability specifications are found by solving the equations of motion for maneuvering. In such equations, hydrodynamic forces and moments are expressed by Taylor expansion as a function of AUV kinetic parameters and a series of constants called hydrodynamic coefficients or derivatives. The constants are divided into two groups: derivatives resulting from the AUVs' velocity, and those of their acceleration. The derivatives of velocity and acceleration relate hydrodynamic forces and moments to the velocity and acceleration of an AUV, respectively. It is necessary to apply a reliable method for estimating hydrodynamic derivatives so as to reduce design costs while improving AUV performance even in pre-construction phase. Hydrodynamic derivatives can be determined via four types of methods: analytical, semi-empirical, numerical and experimental methods. An analytical method can well predict the hydrodynamic derivatives relating to acceleration. However, due to elimination of viscosity effects, it may not work well when calculating velocity derivatives. Semi-empirical methods may not address highly complicated geometries. The most reliable methods are proved to be experimental ones. The most common experimental method is conducting static and dynamic captive model tests in towing tanks and water channel (Julca Avila *et al.* 2012; Zhang and Zou 2013; Krishnankutty 2014). These tests include straight line, rotating arm, and planar motion mechanism tests. They are time-consuming tests to be undertaken in cost-intensive facilities, making them economically non-feasible for preliminary design phase. Computational fluid dynamics (CFD) methods not only are not as difficult, cost-intensive, and time-consuming as experimental methods, but also do not need any PMM equipment. Compared to analytical and semi-empirical methods, CFD methods are seen to be more applicable yet accurate. In a CFD method, static and dynamic captive model tests are simulated in order to estimate hydrodynamic derivatives.

Straight line tests are used to estimate linear and non-linear derivatives coming from linear velocity. Steady CFD methods are applied based on Reynolds Averaged Navier-Stokes (RANS) equations to simulate straight line tests. Bellevre *et al.* (2000) employed a translational and rotational

model based on RANS in the steady state to estimate velocity hydrodynamic derivatives. Wu *et al.* (2005) simulated the straight line tests for SUBOFF model with or without an angle of attack close to the infinite level bottom model. This study assessed the effects of the motion-near-bottom on hydrodynamic forces. Using RANS, Tyagi and Sen (2006) evaluated the coefficients related to transverse velocity. Barros *et al.* (2008) developed a numerical technique to estimate force coefficients from underwater hulls with different angles of attack. CFD results were compared to semi-empirical and empirical results. Among other dynamic model tests, PMM tests are seen to be more useful as they provide required data for estimating velocity and acceleration derivatives. In CFD, unsteady RANS equations are applied to simulate PMM tests. Considering the effects of free surface and using a CFD parallel code, Broglia *et al.* (2007) studied the flow around KVLCC2 tanker during a pure swaying maneuver. With respective relative errors of 5.5 and 20 percent, lateral forces and yaw moment calculated by this method were found to be well corresponded to experimental data. Philips *et al.* (2007) used unsteady RANS modeling of PMM test for Autosub model to estimate velocity and acceleration derivatives. Zhang *et al.* (2010) proposed a new method for simulating hydrodynamic coefficient tests using FLUENT CFD. They applied calculated hydrodynamic coefficients to create a hydrodynamic model. Malik *et al.* (2013) simulated PMM test by CFD for an elliptical axisymmetric geometry of 1:6 scale. They achieved highly accurate results using Fluent along with active meshing and zoning of the computational field to perform pure heave and pitch motions. Generating low-volume and high-quality grid for an AUV body along with wings to simulate static and dynamic captive model tests renders both cost-intensive and time-consuming. With unstructured grids, the number of cells in computational domain increases reducing the quality of meshing around AUV wings and body. Increased number of cells in unsteady simulation would necessitate the use of a powerful probably expensive processor. Low-quality meshing can generate serious problems in the estimation of hydrodynamic coefficients.

To reduce the incurred cost of calculations, this paper presents a numerical modeling approach, based on captive model tests, for the estimation of hydrodynamic derivatives of body and wing. In such an approach, wing and body are individually simulated. The paper is organized in three main sections: the first section introduces AUV model and the theory of estimating hydrodynamic

derivatives; the second section presents the CFD modeling details; and the third section submits conclusion and compares the results with experimental data.

2. AUV MODEL AND TYPES OF TESTS

To calculate hydrodynamic derivatives of an AUV, the dynamic equations of the rigid body should be extracted (Fossen 1994). The HydroLab 500, which can be seen in Fig. 1, is an optimally-designed AUV designed and developed in Iran University of Science and Technology for investigation purposes. It is controlled by four wings located at the end of it in cross shape.

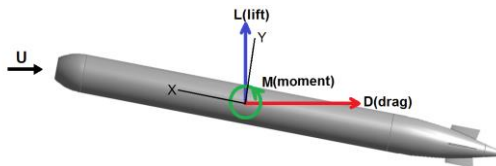


Fig. 1. HydroLab 500 and the coordination system.

Space-fixed and body-fixed coordinate systems are employed to describe the dynamic equations. Assuming that the AUV moves just in the ZX plane, the motion equations can be described as follows (Philips *et al.* 2007):

$$X = mu \tag{1}$$

$$Z = mw + m x_G \dot{q} + (m.U)q \tag{2}$$

$$M = (m x_G) \dot{w} + (I_{yy}) \dot{q} + (m x_G.U).q \tag{3}$$

w and \dot{w} are the linear velocity and acceleration, and q and \dot{q} are the angular velocity and acceleration, respectively. U is the initial velocity, m is the mass of AUV, I_{yy} is the mass moment of inertia about y-axis, and x_G is the coordinates of center of gravity in x-direction. M , Z and X are external forces and moments imposed to AUV, which can be divided into hydrostatic, control, propulsion, and hydrodynamic ones. In dynamic equations, hydrodynamic forces and moments can be expressed as a function of kinematic parameters and a series of constants known as hydrodynamic coefficients or derivatives, by using Taylor series. The heave force and moment resulting from hydrodynamic effects of flow are:

$$Z_H = Z_w w + Z_{\dot{w}} \dot{w} + Z_{|w|} |w| + Z_q q + Z_{\dot{q}} \dot{q} + Z_{q|q} |q| \tag{4}$$

$$M_H = M_w w + M_{\dot{w}} \dot{w} + M_{|w|} |w| + M_q q + M_{\dot{q}} \dot{q} + M_{q|q} |q| \tag{5}$$

Where Z_w , $Z_{|w|}$, M_w , and $M_{|w|}$ are estimated by straight line runs and $Z_{\dot{w}}$, Z_w , M_w , $M_{\dot{w}}$, Z_q , $Z_{\dot{q}}$, M_q and $M_{\dot{q}}$ are estimated by PMM runs.

2.1 Straight Line Tests

In straight line (static) tests, the model is located under a given angle with respect to the flow. The linear and angular acceleration are zero in these tests, so Eqs. 4 and 5 can be rewritten as follows:

$$Z'_H = Z'_w w' + Z'_{|w|} |w'| \tag{6}$$

$$M'_H = M'_w w' + M'_{|w|} |w'| \tag{7}$$

$w' = \sin \alpha = \frac{w}{U}$, Z'_H and M'_H are the non-dimensional form of Z_H and M_H , which have been non-dimensional by $\frac{1}{2} \rho U^2 L^2$ and $\frac{1}{2} \rho U^2 L^3$.

L is the model length of the HydroLab 500, U is the AUV velocity, and ρ is the flow density. Hydrodynamic coefficient due to velocity of AUV can be calculated by static runs. Shear stress and pressure distribution produce hydrodynamic forces and moments over the AUV surface. The resulting force is divided into lift (L) and drag (D) forces that are parallel and perpendicular to the free flow velocity, respectively (Fig.1). The force imposed on the body in the direction perpendicular to the longitudinal axis is equal to:

$$Z = D \sin \alpha + L \cos \alpha \tag{8}$$

2.2 PMM Maneuvers

PMM tests are divided into pure heave and pure pitch motions. As it can be seen in Fig. 2, the model is subjected to a harmonic motion with constant amplitude and frequency in the pure heave tests. Such motion is consisted of a harmonic oscillation along z axis and a forward velocity U. Considering that the model is passing a sine route, the pitch angle θ , angular velocity q and the angular acceleration \dot{q} would be equal to zero at all times. Vertical displacement z , vertical velocity w and vertical acceleration \dot{w} for pure heave motion are as below:

$$\begin{aligned} z &= z_o \sin \omega t \\ w &= \dot{z} = z_o \omega \cos \omega t \\ \dot{w} &= \ddot{z} = -z_o \omega^2 \sin \omega t \end{aligned} \tag{9}$$

Where z_o and ω are the amplitude and circular frequency of the heave motion of AUV model, respectively. Considering pure heave motion ($\theta = q = \dot{q} = 0$) regardless of nonlinear effects, Eqs. 4 and 5 can be rewritten as follows:

$$Z_H = Z_w \dot{w} + Z_w w \tag{10}$$

$$M_H = M_w \dot{w} + M_w w \tag{11}$$

Substituting z , w and \dot{w} from Eq. 8 in Eqs. 9 and 10, we have:

$$Z_H = Z_w \left(-z_o \omega^2 \sin \alpha t \right) + Z_w \left(z_o \omega \cos \alpha t \right) \quad (12)$$

$$M_H = M_w \left(-z_o \omega^2 \sin \alpha t \right) + M_w \left(z_o \omega \cos \alpha t \right) \quad (13)$$

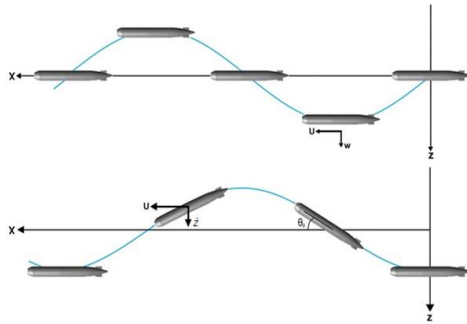


Fig. 2. Pure heave and pitch maneuvers.

In pure pitch test (see Fig. 2), the desired motion is consisted of a harmonic motion in the direction of z axis, a forward velocity U and a harmonic motion for changing the angles. The velocity along x is U and along z , in the inertial coordinate is \dot{z} . According to Fig. 3, the resultant velocity w is tangent to the movement direction of AUV. This motion can be observed as a pure pitch motion in the body-fixed coordinate system, in which, the resultant linear velocity w and the resultant linear acceleration \dot{w} equal with zero. For pure pitch motion we have:

$$\begin{aligned} \theta &= \theta_o \sin \alpha t \\ q &= \dot{\theta} = \theta_o \omega \cos \alpha t \\ \dot{q} &= \ddot{\theta} = -\theta_o \omega^2 \sin \alpha t \end{aligned} \quad (14)$$

θ_o is the angular amplitude of pure pitch motion. For pure pitch motion $w = \dot{w} = 0$, Eqs. 4 and 5 are rewritten as follows:

$$Z_H = (Z_{\dot{q}}) \dot{q} + (Z_q) q \quad (15)$$

$$M_H = (M_{\dot{q}}) \dot{q} + (M_q) q \quad (16)$$

Substituting θ , q and \dot{q} from Eq. 14 in Eqs. 15 and 16, the following equations are obtained:

$$Z_H = (Z_{\dot{q}}) \left(-\theta_o \omega^2 \sin \alpha t \right) + (Z_q) \left(\theta_o \omega \cos \alpha t \right) \quad (17)$$

$$M_H = \left(-\theta_o \omega^2 \sin \alpha t \right) + (M_q) \left(\theta_o \omega \cos \alpha t \right) \quad (18)$$

External force Z_H and external moment M_H measured in pure heave and pitch tests can be decomposed by Fourier analysis into in-phase and out-of-phase components.

$$Z_H = Z_{out} \sin \alpha t + Z_{in} \cos \alpha t \quad (19)$$

$$M_H = M_{out} \sin \alpha t + M_{in} \cos \alpha t \quad (20)$$

Equating the coefficients of sine and cosine

functions in Eqs. 19 and 20 with Eqs. 12 and 13, respectively, and using least square method, Z_w , $Z_{\dot{w}}$, M_w and $M_{\dot{w}}$ can be estimated. Similarly, Z_q , $Z_{\dot{q}}$, M_q and $M_{\dot{q}}$ can be estimated by equating the coefficients of sine and cosine functions in Eqs. 19 and 20 with Eqs. 17 and 18 and using least square method.

3. NUMERICAL PROCEDURE

3.1 Mathematical Equations

The flow around the model is resolved based on RANS. Assuming the fluid to be incompressible, the flow equations are as follows:

$$\begin{aligned} \left(\frac{\partial U_i}{\partial t} \right) + U_j \frac{\partial U_i}{\partial x_j} = -\frac{1}{\rho} \frac{\partial P}{\partial x_i} \\ + \frac{\mu}{\rho} \frac{\partial}{\partial x_j} \left(\frac{\partial U_j}{\partial x_i} + \frac{\partial U_i}{\partial x_j} \right) + \frac{1}{\rho} \frac{\partial}{\partial x_j} \left(\overline{-u'_i u'_j} \right) \end{aligned} \quad (21)$$

where ρ is the density; P is the Reynolds-averaged pressure; U and u refer to the fluid mean and fluctuation velocity components, respectively; μ is the fluid dynamic viscosity; $\overline{u'_i u'_j}$ indicates fluid Reynolds stresses; and $k - \varepsilon$ is the turbulence model applied to calculate the Reynolds stresses. $k - \varepsilon$ is one of the most commonly used models in aerodynamic and hydrodynamic flows. Corresponding equations to $k - \varepsilon$ areas follows:

$$\frac{\partial}{\partial t} (\rho k) + \nabla \cdot (\rho k U) = \nabla \cdot \left[\left(\mu + \frac{\mu_t}{\sigma_k} \right) \nabla k \right] + P_k - \rho \varepsilon \quad (22)$$

$$\begin{aligned} \frac{\partial}{\partial t} (\rho \varepsilon) + \nabla \cdot (\rho \varepsilon U) = \nabla \cdot \left[\left(\mu + \frac{\mu_t}{\sigma_\varepsilon} \right) \nabla \varepsilon \right] \\ + \frac{\varepsilon}{k} (C_{1\varepsilon} P_k - C_{2\varepsilon} \rho \varepsilon) \end{aligned} \quad (23)$$

Where,

$$P_k = \mu_t \nabla \cdot (\nabla U + \nabla U^T) + \frac{2}{3} \nabla \cdot U [3 \mu_t \nabla \cdot U + \rho k] \quad (24)$$

$$\mu_t = C_\mu \rho \frac{k^2}{\varepsilon} \quad (25)$$

In the above equations, k is the turbulent kinetic energy, ε denotes the viscous dissipation rate of turbulent kinetic energy, μ_t represents eddy viscosity with $C_{1\varepsilon}$, $C_{2\varepsilon}$, C_μ , σ_k , and σ_ε being model constants which take different values for different models. The realizable $k - \varepsilon$ model (high-Re) (Shih *et al.* 1999) was used for modeling the turbulence flow. The realizable $k - \varepsilon$ model contains a new formulation for the turbulent

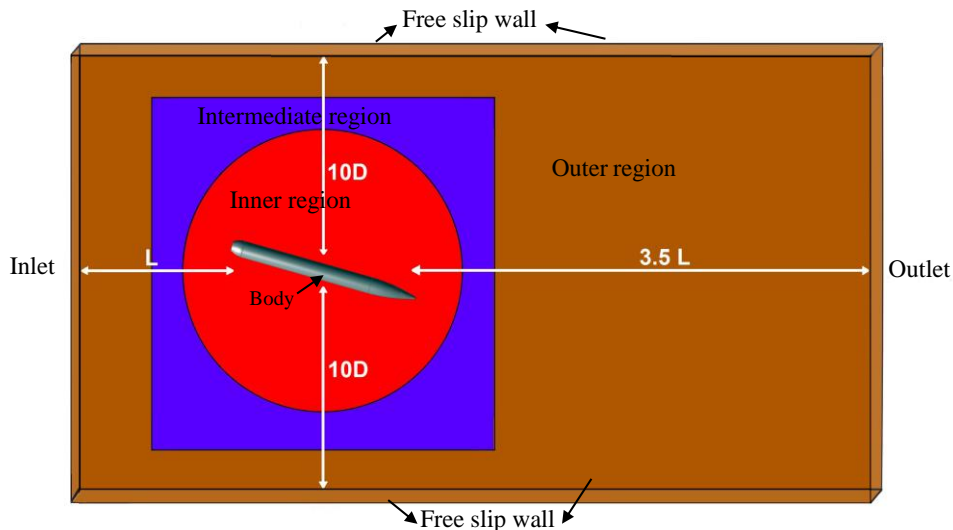


Fig. 3. The model designed for the body to do meshing and conducting straight line and PMM tests.

viscosity and a new transport equation for the dissipation rate, ε , that is derived from an exact equation for the transport of the mean-square vorticity fluctuation. It introduces a variable, rather than a constant, C_μ . Better performance in flows involving rotation, boundary layers under strong adverse pressure gradient, flow separation, and recirculating flows are enumerated as a few advantages of the realizable $k-\varepsilon$. In addition to its ability to dynamically update the viscosity, and the use of modified transport equation for ε , the realizable $k-\varepsilon$ can effectively model all the effects of the boundary layer including the close-to-wall phenomenon.

3.2 Geometrical Modeling and Boundary Conditions

To estimate hydrodynamic derivatives of HydroLab 500, numerical modeling of captive model tests was separately done for the wing and the body. The whole domain was completely planned before meshing, so as to save time. Fig. 3 shows the model designed for the body to do meshing followed by straight line and PMM tests. The wings of the original model are located downstream of the model with the volume ratio of the wings to the body been small. Thus, interference effects of the wings on the body could be adequately ignored (Barros *et al.* 2008). The computational domain was broken into three parts of inner, intermediate and outer regions for performing angular and linear motions. The body of HydroLab 500 was encompassed within the inner region which is sphere-shaped. The inner region could rotate relative to the outer and intermediate regions in order to make the required angular changes. A linear motion was applied to the cube-shaped inner and intermediate regions. Fig. 3 illustrates the dimensions of the computational domain. The boundary conditions were applied to the outer region and HydroLab 500 body. The velocity inlet boundary condition and the outlet

pressure were applied to the front and rear boundaries, respectively. No-slip condition was allowed over the body of HydroLab 500. Zero vertical velocity gradients were taken for the upper, lower, and side surfaces.

Figure 4 presents the model designed for the wings to do meshing and conducting straight line and PMM tests. Likewise, the computational domain was divided into three parts of inner, intermediate, and outer regions to apply angular and linear motions. Regarding the interaction effects of body over wing flow, the wing was assumed to be fixed to the wall in the inner region. The angular and linear motions were applied by sphere and cube to the wing and fixed wall, respectively. The boundary conditions were applied to the outer region and the surface of the wing and the wall fixed to it. The velocity inlet boundary conditions and the outlet pressure were applied to the front and rear boundaries, respectively. Non-slip condition was employed for the wing surface and the wall fixed to it. Zero vertical velocity gradients were used for the upper, lower, and first side surfaces. For the second side surface, the symmetry condition was considered. By applying suitable maneuvers to the inner and intermediate regions, pure heave and pitch motions at the desired amplitudes and frequencies are possible.

3.3 Meshing and Grid Independence

In this study, a structured grid of hexahedral cells was applied to all areas. Results from the numerical study were highly depended on the meshing parameters. Fig. 5 illustrates meshing around the body. Nodes around the whole AUV are distributed along the hull, so that the flow close to the body is better resolved. Fig. 6 shows meshing around the wings. At the end of the body, due to the formation of recirculating flows and a wake, the cells are more compressible. Due to the complication of flow

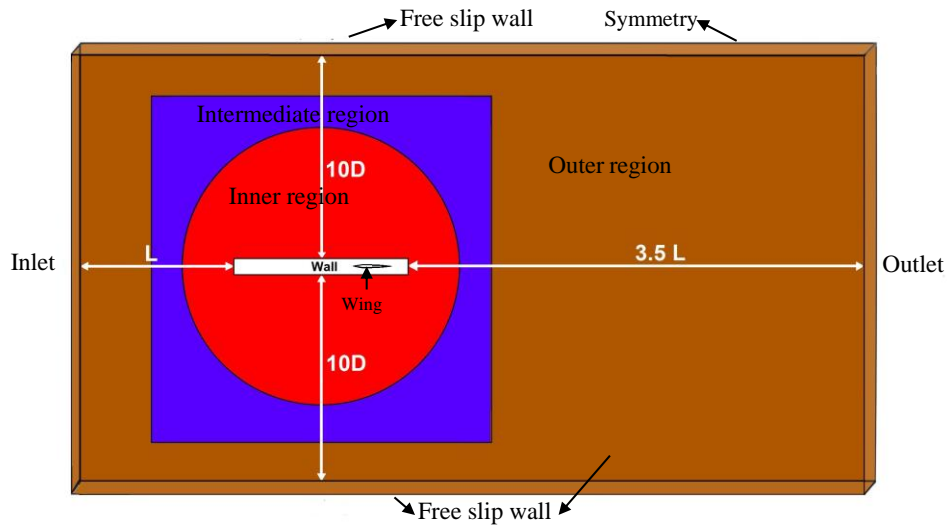


Fig. 4. Model designed for the wing to do meshing and conducting straight line and PMM tests.

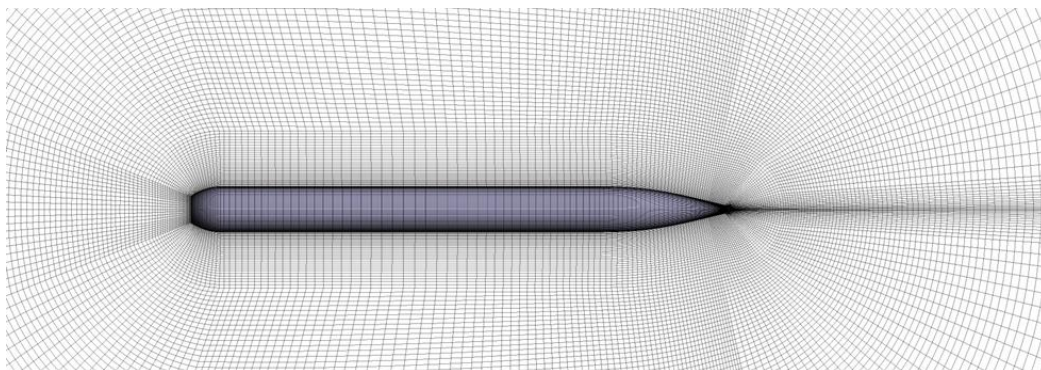


Fig. 5. Meshing around the model body.

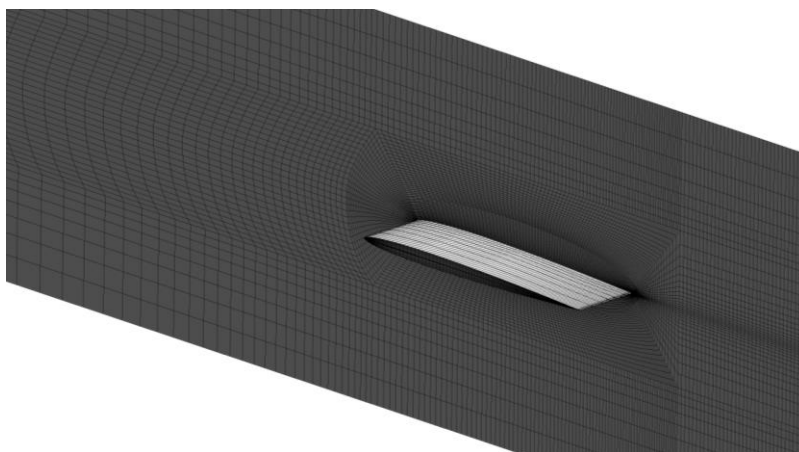


Fig. 6. Meshing around the wings.

around the wings, higher accuracy was incorporated into the meshing within thin region. Skewness refers to the shape difference of cells with an equilateral cell in the equivalent volume. The most difficult region for reducing skewness was the region encompassing the wings. Near the body wall and the wings, the skewness was satisfyingly below

0.43. However, going away from the wall, the mean skewness was seen to be reduced.

Before analyzing CFD, solving sensitivity to the grid should be considered. Accordingly, four grids were generated to study the independence from the meshing at all Reynolds numbers. For example,

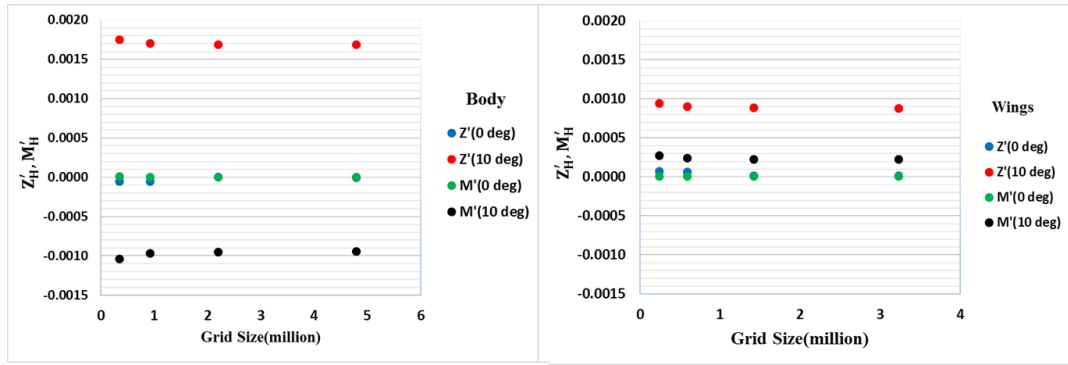


Fig. 7. Sensitivity of hydrodynamic parameters to grid size changes across the body and the wing.

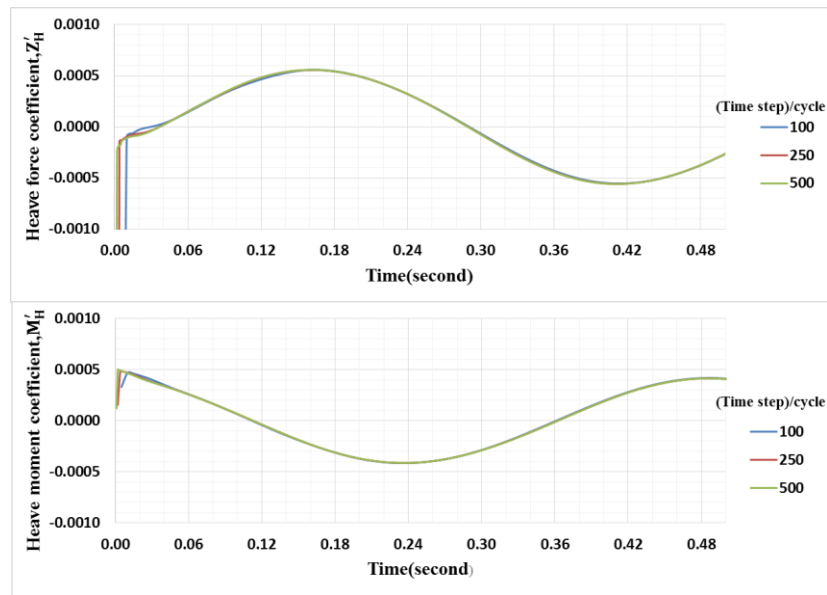


Fig. 8. Variations in heave force and moment coefficients with varying time steps.

Figure 7 shows the meshing details used to study the dependency of the solution to the grid at $Re = 2 \times 10^6$. A grid is chosen as the initial grid. Grids for the inner region were refined using the ratio of $\sqrt{2}$ in each direction toward the previous grid (R ITTC 1999). The refinement ratio for outer region was less than $\sqrt{2}$. The meshing number varied between 0.357 - 4.796 and 0.248 - 3.231 million grids for the body and the wing, respectively. y^+ was the non-dimensional distance from the wall to the closest node to the wall, which represented the accuracy of the numerical predication. For a realizable $k - \epsilon$ model with a standard wall function, y^+ is required to be within 30 to 300. Here, y^+ varied from 30 for the finest grid to 80 for the coarsest one. The convergence test was conducted with its focus on force and moment coefficients imposed on the body and the wings at 0 and 10-degree angles. The SIMPLE algorithm was used for pressure-velocity coupling. A second order upwind scheme was applied to discretize momentum, turbulence kinetic energy and a

turbulence dissipation rate in all the computations. The convergence criteria were set to 10^{-6} for all the residues. No significant difference was observed for the force and moment coefficients of body in grids 3 and 4. Also, no significant difference was observed for the drag and lift coefficient of the wing in grids 3 and 4. Considering the calculation cost, grid 3 (with 2.205 and 1.426 million cells for the designs of the body and the wings, respectively) was selected for the calculations of the body and the wing.

It is necessary to estimate a time step for unsteady simulation, so as to reach reliable results and minimize time duration. To investigate the effect, simulations were implemented at three time steps, namely 100, 250, and 500, with courant numbers of 4, 1.6, and 0.8, respectively, for one oscillation. For example, results of pure heave motion for the body have been presented in Fig. 8. Some instabilities were observed in time steps at 1/8 oscillation primary cycles. Courant number below 1 is seen to be good for unsteady problems. In this study, as the oscillations are small, the number of time steps

could be reduced. Here, the number of time steps per oscillation varied from 250 to 500 for various frequencies.

4. VALIDATION

To validate the CFD results, several experimental tests were done on HydroLab 500 in $Re = 2 \times 10^6$ in the water tunnel. Fig. 5 shows the set-ups for doing the experimental runs. The system helped carrying out static tests including straight line and dynamic tests including pure pitch, pure heave and the combination of pure pitch and heave motions in water tunnel. It was applied to estimate the derivatives of velocity and accelerations. Straight line Tests were done at attach angles ranging from -6 to 6 degrees at an increment of 2° at $Re = 2 \times 10^6$. Pure heave tests were conducted at different frequencies (0.5-2.25 Hz) and amplitudes (1-3 cm). All tests were conducted at $Re = 2 \times 10^6$. Forces and moments were measured by a 6-component strain gauge balance (Nouri *et al.* 2014) located in the HydroLab 500 model. The six-component balance has been calibrated with maximum error of 0.1%.

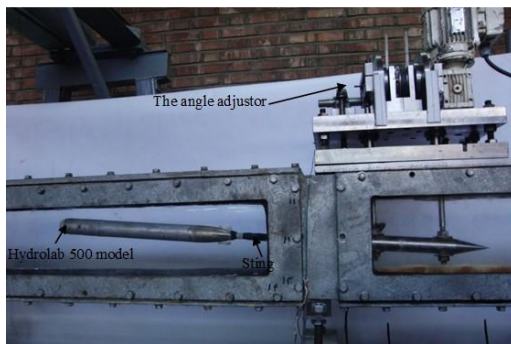


Fig. 9. Experimental set-up installed in water tunnel to implement of static and dynamic tests.

5. NUMERICAL SIMULATION RESULTS

Captive model tests for the wing and the body of HydroLab 500 were individually simulated to estimate hydrodynamic coefficients. To validate the CFD results, there are only an apparatus capable of performing straight line and PMM tests in the water tunnel of IUST at Reynolds number values less than 3×10^6 for estimating the AUV hydrodynamic coefficients, based on the planar experiments. Therefore, CFD modeling was performed to simulate captive model tests including straight line and planar motion mechanism (PMM) at $Re = 2 \times 10^6$. Total forces and moments were set equal to the sum of those on the wing and the body.

5.1 Straight Line Tests

Such simulations were conducted to obtain hydrodynamic coefficients related to AUV linear velocity. HydroLab 500's angle of attack was changed, in two-degree steps, from -10 to 10 using the sphere planned in the numerical model. For instance, the distribution of velocity contours at 6° angle of attack is depicted in Fig. 10 for the body

and the wing. Due to the angle of attack, the streamline is deviated toward the upper half of the wing and the body. The deviation is as a result of the cross flow. With increased angle of attack, there was probably a separation in the upper half of the body and wing. Lift (L) and drag (D) forces were calculated by integrating the pressure distribution and shear stress. To calculate total forces and moments of the four wings of the AUV, the values achieved at zero angle of attack (corresponding forces and moments to vertical wings) were added to simulation results at each pitch angle (corresponding forces and moments to horizontal wings). The normal force Z was then calculated by the Eq. 8.

Figure 11 shows the total coefficients of vertical

$$\text{force } Z' = \frac{Z_H}{\rho L^2 U^2} \text{ and moment } M' = \frac{M_H}{\rho L^3 U^2}$$

from the sum of wings and body around the mass center of AUV based on non-dimensional vertical velocity $w' = \frac{w}{U} = \sin \alpha$. To compare the wings

and total values, it was found that loads due to the wings are significant. Therefore, wings effect must be considered to estimate the hydrodynamic derivatives. By matching Eqs. 6 and 7 to the data appeared above Diagram 11, derivatives $Z'_{w'|w|}$, $Z'_{w'|w|}$, $M'_{w'|w|}$, and $M'_{w'|w|}$ were estimated by least squares and regression methods. The linear components $Z'_{w'|w|}$ and $M'_{w'|w|}$ were defined as the effects of potential flow, and $Z'_{w'|w|}$ and $M'_{w'|w|}$ were defined as the viscous effects.

Table 1 lists estimated linear and nonlinear derivatives and the difference, in percentage, from the experimental method relating to vertical force and the pitch moment. If $Z'_{w'|w|}$ and $M'_{w'|w|}$ are considered to be a result of damping effect related to flow separation, than the magnitude of this should be larger for the model where the separation occurs. $Z'_{w'|w|}$ and $M'_{w'|w|}$ obtained by experimental tests were greater than values estimated via numerical simulations. This could be due to the effects of experimental equipment on the model flow in experimental tests. The differences estimated between the numerical model results and the experimental data ranged from 6-13 percent. The numerical method has succeeded to estimate linear derivatives more accurately than nonlinear derivatives. This might be because of the dependency of linear derivatives on the AUV geometry along with the lower sensitivity of the applied model than the turbulence model. Consider now the moment coefficients The Munk moment (Newman, 1977) is always destabilizing as it tends to turn the vehicle perpendicular to the flow. On the other hand, for viscous flow over the body, a boundary layer is formed which eventually separates over a region near the trailing edge. While this causes an additional drag, the nature of the resulting moment is generally stabilizing and thus

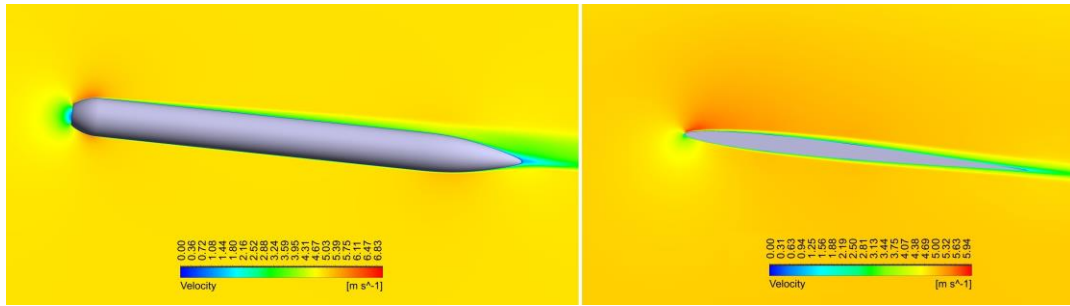


Fig. 10. Distribution of velocity contours for the wing and the body at 6° angle of attack.

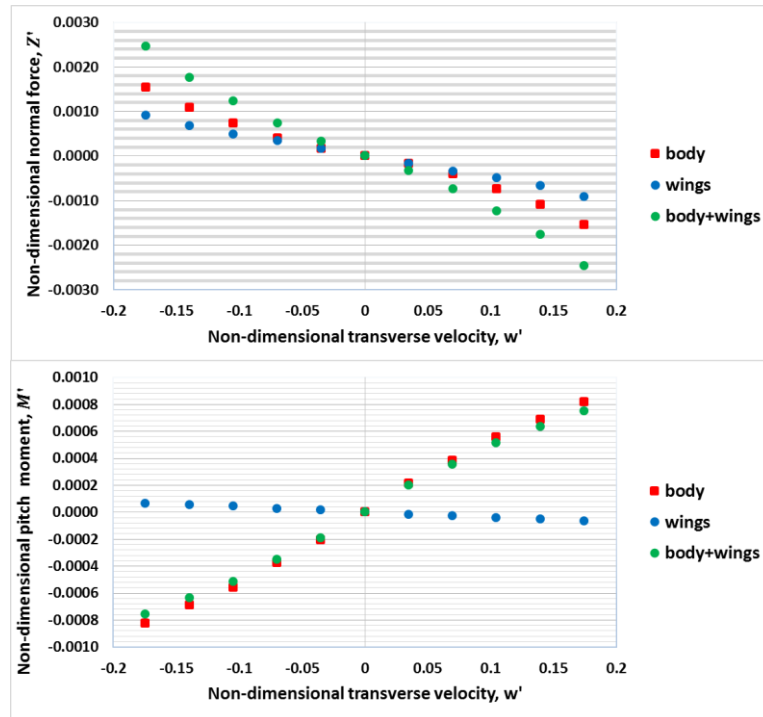


Fig. 11. Coefficient of vertical force and pitch moment based on non-dimensional velocity.

opposite to the nature of the Munk moment. These two competing moments eventually decide the overall direction of the moment. As can be seen here, the linear coefficient and $M'_{w'}$, the nonlinear coefficient $M'_{w'|w'|}$ show opposite sign, and therefore support the conjecture that the former (the linear part) is the Munk moment arising from inviscid flow effect, and the nonlinear part represents the effect due to viscosity.

Table 1 Hydrodynamic derivatives estimated by straight line tests

Coefficients	Hydolab 500(CFD)	Hydolab 500(EXP)	Error (%)
$Z'_{w'}$	-0.0102781	-0.010962	6.2
$M'_{w'}$	0.005225	0.005651	7.5
$Z'_{w' w' }$	-0.009082	-0.009983	9
$M'_{w' w' }$	-0.0029	-0.00331	12.3

5.2 PMM Tests

In a pure heave maneuver, the model moves in a sine route and all along the way, AUV's longitudinal axis is parallel to the direction of water flow. Therefore, forces and moments are independent of the angular motion. To create a pure heave maneuver for the wing and the body, Eq. 9 was used with inner and intermediate regions shown in Figs. 3 and 4, respectively. Pure heave tests were conducted at different frequencies (0.5-2.25 Hz) and amplitudes (1-3 cm). As an example, an instantaneous representation of velocity distribution for the wing and the body is depicted in Fig. 12 at different times. Taking account of the quasistationary nature of mathematical maneuvering models, numerical data should not be affected by memory effects due to the application of nonstationary techniques. Regarding Fig. 12, due to the oscillations, the wake generated behind the model represents an oscillatory pattern. It is the in-phase of object motion and along the axis. It can be

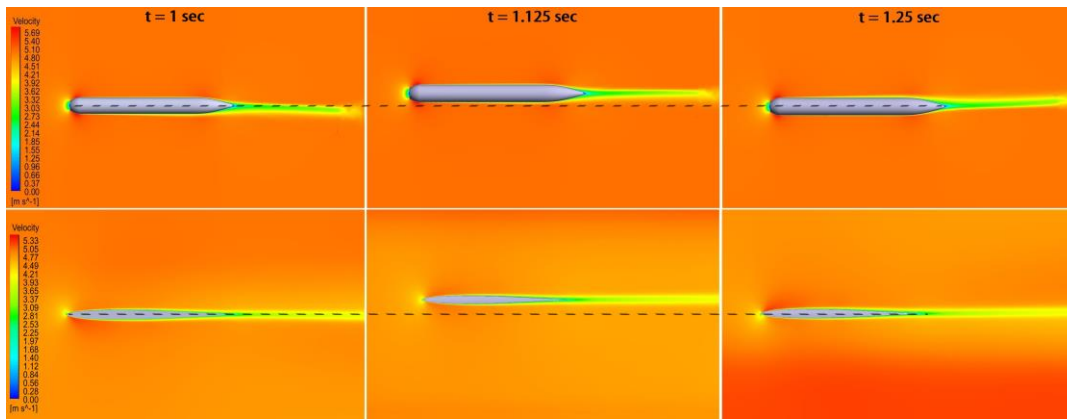


Fig. 12. Velocity distribution based on time for the body and the wing during pure heaving test ($f=2$ Hz).

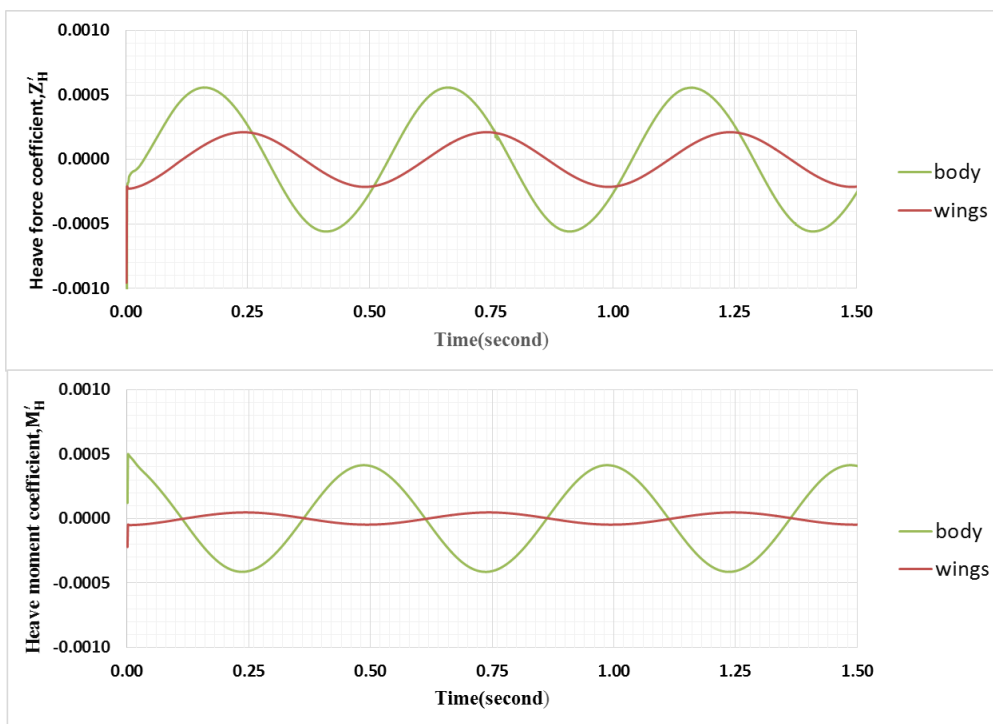


Fig. 13. Force and moment coefficients acting on the body and the wings during pure heaving test ($f=2$ Hz).

concluded that the realistic motion was imposed on the wing and body. Therefore, the hydrodynamic coefficients aren't affected by memory effects in the selected conditions, which can be ascribed to wake interference. Fig. 13 shows the chronology of changes in force and moment coefficients which are active over the body and the wing in three complete cycles in the pure heave maneuver. Using Fourier expansion for the resulting data, sine and cosine coefficients in Eqs. 19 and 20 were estimated separately for the wing and the body. Used in Fourier expansion was the corresponding data to the two ending cycles. Forces and moments of linear velocity and acceleration were separated by a fitted equation. Forces and moments relating to the linear velocity of the vertical wings were considered by adding the values calculated by static simulations in

zero angle. As the acceleration forces were depended on the wing geometry, by doubling the sine coefficients estimated by Fourier series for the wings, forces and moments of vertical wing accelerations were considered in the real model. The resulting coefficients were equal to the sum of coefficients of the wings and the body.

The slope of the first-order equation estimated for the data of the coefficient of forces $\frac{Z_H}{\frac{\rho L^2 U z_0}{2}}$ and

the coefficients of moment $\frac{M_H}{\frac{\rho L^3 U z_0}{2}}$ resulting from

the velocity (in-phase with speed) for the sum of

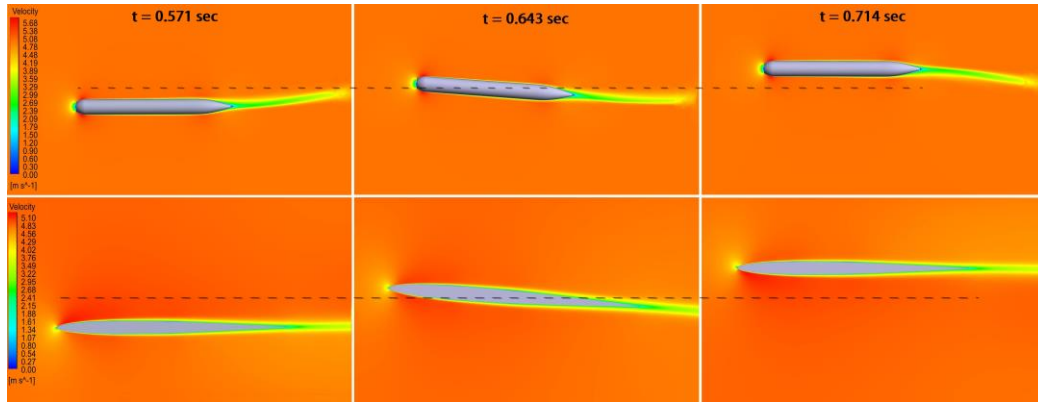


Fig. 14. Velocity distribution with respect to time for pure pitch motion simulation of the body and the wings.

wings and body based on frequency ω show the non-dimensional hydrodynamic derivatives Z'_w and M'_w . The slope of the first-order equation for

the coefficient of forces $\frac{Z_H}{\frac{\rho L^3}{2} z_0}$ and the

coefficients of moment $\frac{M_H}{\frac{\rho L^4}{2} z_0}$ for the sum of

wing and body based on ω^2 having 90 degree phase difference with velocity indicates the non-dimensional hydrodynamic derivatives Z'_w , and M'_w . The least squared regression was used to approximate the first-order equation. Table 2 presents coefficients estimated by CFD relating to pure heave motion along with experimental results.

Table 2 Hydrodynamic derivatives estimated by pure heave maneuver

Coefficients	Hydrolab 500(CFD)	Hydrolab 500(EXP)	Error (%)
Z'_w	-0.010571	-.0117417	10.0
Z''_w	-0.01002	-0.0103415	3.1
M'_w	0.005441	0.005959	8.7
M''_w	0.006102	0.00641	4.8

The differences estimated using the numerical model with the experimental tests is ranges from 3-10 percent. As observed in the table, the estimation error for the acceleration derivatives is smaller than other derivatives. Such coefficient is trivially affected by the viscosity effects and the modeling errors relating to the turbulence flow and more depends on the pressure distribution around the model.

In the pure pitch maneuver, the recorded forces and moments are independent of the linear motion. In this maneuver, the linear velocity \dot{z} , in the Eq. 9, was applied to the inner and intermediate regions, and the angular velocity $\dot{\theta}$, in the Eq. 14, was applied to the inner region. Pure pitch runs were

conducted with different frequencies (1.5-3.5 Hz), in the amplitudes of 1 to 3 cm for vertical displacement, and 4 to 8 degree for angular changes. Memory effects can be explained by interference between the model's swept path and its own (lateral) wake, leading to unrealistic flow. As an example, Fig. 14 shows velocity contours with wake generated behind the wings and body for different times. It can be concluded that the realistic motion was imposed on the wing and body. Therefore, the hydrodynamic coefficients aren't affected by memory effects in the selected conditions, which can be ascribed to wake interference. Fig. 15 depicts the chronology of changes in forces and moments which are active over the body and wing in three complete cycles in the pure pitch maneuver, forces and moment coefficients of angular velocity and acceleration were separated using Fourier expansion and Eqs. 19 and 20. Forces and moments relating to the angular velocity of vertical wings were considered by adding the values calculated by static simulations in same angle with the angular amplitude of pure pitch motion. Forces and moments relating to the angular velocity of vertical wings were considered by doubling the sin coefficients estimated by Fourier series for wings. The resulting coefficients equal to the sum of coefficients of wings and body.

The slope of the first-order equation estimated for the data $\frac{Z_H}{\frac{\rho L^2 U^2 \theta_0}{2}}$ and the moment coefficient

$\frac{M_H}{\frac{\rho L^3 U^2 \theta_0}{2}}$ resulting from the velocity (in-phase with

speed) for the sum of the wing and the body based on frequency ω showed the non-dimensional hydrodynamic derivatives $Z'_{q'}$ and $M'_{q'}$, respectively. The slope of the first-order equation for the coefficient of forces $\frac{Z_H}{\frac{\rho L^4}{2} \theta_0}$

coefficients of moment $\frac{M_H}{\frac{\rho U L^2}{2} \theta_0}$ resulting from the

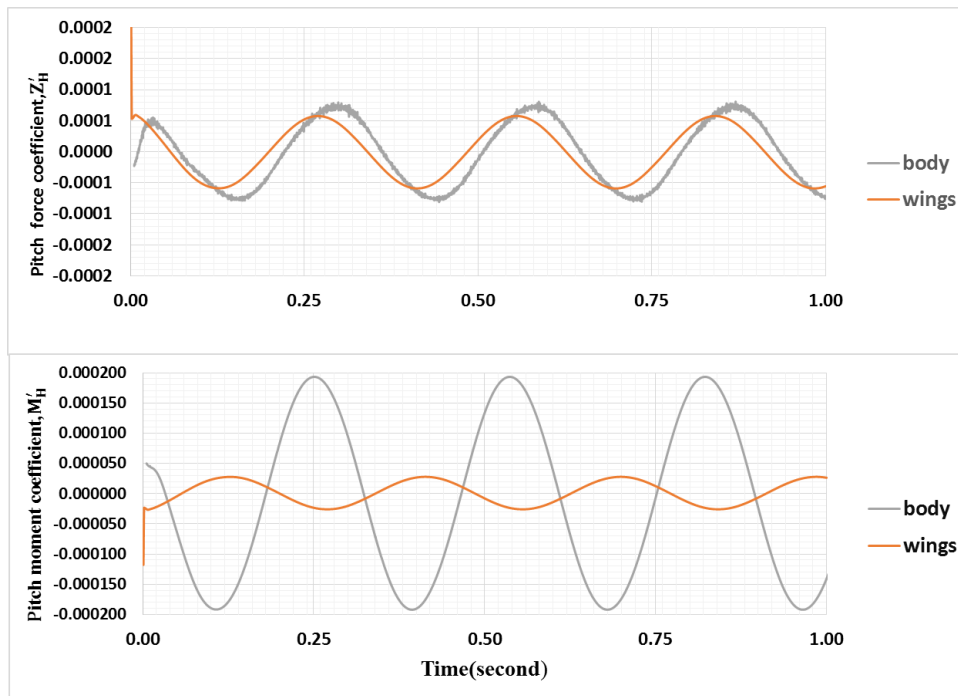


Fig. 15. Force and moment acting on the body and the wings during pure heave motions ($f=3.5\text{Hz}$).

velocity (in-phase with speed) for the sum of the wings and the body based on ω^2 indicated the non-dimensional hydrodynamic derivatives $Z'_{\dot{q}}$, and $M'_{\dot{q}}$, respectively. Table 3 presents the derivatives obtained by pure pitch motions.

Table 3 Hydrodynamic derivatives estimated by pure pitch maneuver

$Z'_{\dot{q}}$	$M'_{\dot{q}}$	$Z'_{\dot{q}}$	$M'_{\dot{q}}$
005443	-0.0022352	-0.000473	-0.000631

6. CONCLUSION AND SUMMARY

A numerical method was proposed for the simulation of captive models used to estimate AUVs' hydrodynamic derivatives. In this modeling approach, straight line and PMM tests were separately modeled to estimate the hydrodynamic derivatives for the wing and the body. Calculated values were validated by having them compared to experimental data. Results disclosed that the proposed model was able to estimate the hydrodynamic coefficients of AUVs' body and connected parts at a reasonable level of accuracy. The proposed methodology provided a low-volume, high quality structured meshing for the AUV body. Reduced number of cells in simulation and increased quality of meshing saved time while raising the accuracy of estimations at the same time. The presented model also reduced the calculation costs incurred when estimating required force and moment parameters during the process of AUVs' detail design. It can be used as a model for estimating AUVs' hydrodynamic derivatives.

REFERENCES

- Barros, E. A., L. D. Dantas, A. M. Pascoal and E. de Sa (2008). Investigation of Normal Force and Moment Coefficients for an AUV at Nonlinear Angle of Attack and Sideslip Range. *Journal of Oceanic Engineering* 33, 583-579.
- Bellevre, D., A. Diaz de Tuesta and P. Perdon (2000, September). Submarine Manoeuvrability Assessment Using Computational Fluid Dynamic Tools. In *Proceeding of 23rd Symposium of Naval Hydrodynamics*, Val de Reuil, France,
- Brogli, R., A. D. Mascio and G. A. Amati (2007). Parallel Unsteady RANS Code for the Numerical Simulations of Free Surface Flows. *2nd international Conference on Marine Research and Transportation*, Naples, Italy.
- Fossen, T. I. (1994). *Guidance and Control of Ocean Vehicles*, 2nd Ed., John Wiley and Sons Ltd., New York.
- ITTC quality manual (1999). Uncertainty analysis in CFD and guidelines for RANS codes. *Interim Recommended Procedure Prepared by Resistance Committee of 22nd ITTC*.
- Julca Avila, J., K. Nishimoto, J. C. Adamowski and C. Mueller Sampaio (2012). Experimental Investigation of the Hydrodynamic Coefficients of a Remotely Operated Vehicle Using a Planar Motion Mechanism. *Journal of Offshore Mechanics and Arctic Engineering* 134(2).
- Krishnankutty, P., V. Anantha Subramanian, R. Francis, P. Prabhasudan Nair and K. Sudarsan

- (2014, June). Experimental and Numerical Studies on an Underwater Towed Body. In *Proceedings of the ASME 33rd International Conference on Ocean, Offshore and Arctic Engineering*, San Francisco, CA. 8-13.
- Malik, S. A., P. Guang (2013). Transient Numerical Simulation for Hydrodynamic Derivatives Prediction of an Axisymmetric Submersible Vehicle. *Research Journal of Applied Science, Engineering and Technology*.
- Newman, J. N. (1977). *Marine Hydrodynamic*, MIT Press, Cambridge, Massachusetts, USA.
- Nouri, N. M., M. Mostafapour, M. Kamran and R. Bahadori (2014). Design Methodology of a Six-Component Balance for Measuring Forces and Moments in Water Tunnel Tests. *Measurement* 58, 544–555.
- Phillips, A., M. Furlong and S. R. Turnock (2007). Virtual Planar Motion Mechanism Tests of the Autonomous Underwater Vehicle Autosub. *STG-Conference/Lectureday CFD in Ship Design*, Hamburg, Germany.
- Shih, T., W. Liou, A. Shabbir, Z. Yang and J. Zhu (1999). A New K-Epsilon Eddy Viscosity Model for High Reynolds Number Turbulent Flows. Model Development and Validation. *NASA STI/Recon Technical Report* 95.
- Tyagi, A. and D. Sen (2006). Calculation of Transverse Hydrodynamic Coefficients Using Computational Fluid Dynamic Approach. *Ocean Engineering* 33, 798-809.
- Wu, B. S., X. Fu and X. F. Kuang (2005). Investigation of Hydrodynamic Characteristics of Submarine Moving Close to the Sea Bottom with CFD Methods. *Journal of Ship Mechanics* 73, 19-28.
- Zhang, H., Y. R. Xu and H. P. Cai (2010). Using CFD Software to Calculate Hydrodynamic Coefficients. *J. Marine. Sci. Appl.* 9, 149-15.
- Zhang, X. G. and Z. J. Zou (2013). Estimation Of The hydrodynamic Coefficients From Captive Mode Test Results By Using Support Vector Machines. *Ocean Engineering* 73, 25–31.